

Strontium Speciation during Reaction of Kaolinite with Simulated Tank-Waste Leachate: Bulk and Microfocused EXAFS Analysis

SUNKYUNG CHOI,^{†,‡} PEGGY A. O'DAY,^{*,‡} NELSON A. RIVERA,[‡] KARL T. MUELLER,[§] MURTHY A. VAIRAVAMURTHY,^{||} SUPAPAN SERAPHIN,[‡] AND JON CHOROVER[†]

Department of Soil, Water and Environmental Science, and Department of Materials Science and Engineering, University of Arizona, Tucson, Arizona 85721, School of Natural Sciences, University of California, Merced, California 95344, Department of Chemistry, The Pennsylvania State University, University Park, Pennsylvania 16802, Brookhaven National Laboratory, Upton, New York 11973-5000, and Department of Materials Science and Engineering, University of Arizona, Tucson, Arizona 85721

Radioactive strontium (⁹⁰Sr) is an important constituent of the complex wastes from past nuclear weapons production and has been stored in underground tanks at U.S. DOE sites (e.g., Hanford, WA). Using bulk and microfocused EXAFS spectroscopy, we examined temporal changes in solid-phase Sr speciation in kaolinite samples reacted for 1–369 d with high-pH, high ionic strength synthetic tank-waste leachate containing Sr²⁺ and Cs⁺ at 10⁻³ mol kg⁻¹. Analyses of bulk EXAFS spectra showed that Sr initially forms a precipitate by 7 d with a local structure similar to SrCO₃(s). At 33 d, microfocused EXAFS of individual particles in one sample revealed a mixture of hydrated and dehydrated Sr associated with neoformed sodalite-type phases. At aging times of 93 d and longer, bulk EXAFS spectra and supporting characterizations indicated nonexchangeable Sr with a local structure consistent with incorporation into increasingly crystalline aluminosilicate particles, particularly sodalite. These experimental studies suggest that irreversible trapping of radionuclides occurs if they are present during the formation and aging of feldspathoid alteration products of local Si-bearing sediment minerals. This may serve as an effective contaminant sequestration mechanism at sites such as Hanford.

Introduction

The remediation of radioactive contamination at former weapons testing and production sites is a costly and protracted legacy of the United States' post-WWII military

industrial complex. Cost estimates of the cleanup, stabilization, and monitoring of Hanford and other former nuclear weapons facilities run to several hundred billion dollars over 25–75 years (1). ⁹⁰Sr and ¹³⁷Cs are important contaminants at a number of Department of Energy (DOE) sites, and particularly at the Hanford (WA) site, because their half-lives fall within human time scales (29 and 30 years, respectively), they are potentially mobile in groundwater, and they are bioavailable substituents for Ca²⁺ and K⁺, respectively, in organisms (2). The volume and extent of contamination at Hanford makes it the largest and most expensive of DOE's cleanup operations. Large volumes of high-level radioactive waste and contaminant metals were generated from plutonium production and separation processes, much of which was stored in underground tanks. At least 67 single-shell tanks containing high-level wastes are known to have leaked into vadose zone sediments, where highly alkaline, high ionic strength fluids have reacted with sediment minerals and groundwater to generate a complex history of mineral alteration, fluid evolution, and waste dispersal (3, 4).

The migration behavior of Sr and Cs in the vadose zone and groundwater at Hanford varies considerably across the site (2, 3). Differences in mineral solubilities and sorption affinities for Sr²⁺ and Cs⁺ explain qualitative differences in contaminant transport behavior. Most studies agree that Sr²⁺ generally adsorbs to mineral surfaces as an outer-sphere complex via an ion-exchange mechanism (5–7). However, Sr²⁺ tends to form strong aqueous complexes with dissolved carbonate and possibly forms stable ternary surface complexes with sorbed carbonate (as suggested for the uranium–carbonate system) (6, 8). The low solubility of SrCO₃(s) is believed to influence aqueous Sr²⁺ concentrations under mildly alkaline conditions (9). In contrast, Cs⁺ mobility is restricted by its high affinity for reactive frayed-edge sites on partially weathered mica and illite (10) and by the formation of inner-sphere complexes at charged ditrigonal siloxane sites in 2:1 clays (11, 12). In the vadose zone impacted by leaking underground tanks at Hanford, the extreme chemistry of the waste fluid has driven mineral alteration and secondary mineral formation under chemical conditions not found in surface environments. The initial subsurface conditions, reaction pathways, and reaction rates have influenced the subsequent transport history of radioactive contaminants such as Sr and Cs, but they are mostly unknown in the field. As such, experimental studies have sought to investigate the extent to which caustic waste reactions with soil minerals contribute to stabilization versus enhanced migration of Sr, Cs, and other radionuclides (e.g., refs 13 and 14).

In a series of studies, we examined different specimen clays reacted with synthetic tank-waste leachate (STWL) containing a range of Sr and Cs concentrations (consistent with concentrations up to ppm released to the vadose zone from leaking tanks (3)), and characterized the reaction products with variety of methods (15–18). Our results indicate that Sr is strongly incorporated into secondary solids that form as a result of clay reaction with STWL. Here we report new data on Sr associated with kaolinite reaction products as a function of time as probed by bulk and microfocused EXAFS spectroscopy and supporting characterizations. This analysis, together with previously reported experimental data (17), provides new insight into the chemical evolution of radionuclide Sr under these extreme reaction conditions and supports a mechanistic basis for predicting its future potential fate under natural weathering conditions.

* Corresponding author e-mail: poday@ucmerced.edu; phone: 209-724-4338; fax: 209-724-4459.

[†] Department of Soil, Water and Environmental Science, University of Arizona.

[‡] University of California.

[§] The Pennsylvania State University.

^{||} Brookhaven National Laboratory.

[‡] Department of Materials Science and Engineering, University of Arizona.

Materials and Methods

Sample Preparation. Size fractionated (<2 μm) specimen kaolinite (KGa-2, Clay Minerals Society) was reacted in STWL solution (0.5 g dry mass of kaolinite in 25.0 g solution), composed of ultrapure (MilliQ) water (CO_2 -free) with 2.0 mol kg^{-1} Na^+ , 1 mol kg^{-1} NO_3^- , 1 mol kg^{-1} OH^- , and 0.05 mol kg^{-1} Al_r . Initial Cs^+ and Sr^{2+} concentrations were 10^{-5} , 10^{-4} , or 10^{-3} mol kg^{-1} . Blank controls included STWL solution without kaolinite and STWL solution without kaolinite and Al (to evaluate homogeneous precipitation of carbonate and/or Al-hydroxide). Duplicate batch reactors and controls (60 mL volume polypropylene bottles; ~ 40 mL of air headspace) were placed on an end-over-end shaker at 2 rpm at ambient conditions, and samples were collected after 1, 7, 33, 93, 190, 324, and 369 d. After centrifugation, pellets were cleaned with 95% ethanol (adjusted to pH 10 with 1 M NaOH) and freeze-dried prior to analysis. For stepwise chemical extractions, duplicate samples were re-suspended in 33.0 g of 0.1 M $\text{Mg}(\text{NO}_3)_2$, shaken for 1 h, and then centrifuged to extract weakly bound Cs and Sr. Pellets were washed three times with 95% ethanol prior to being re-suspended in 0.2 M acidic ammonium oxalate solution (AAO) (4 h at pH 3 on a reciprocal shaker in the dark) to extract “poorly crystalline” precipitates. Bulk Sr concentrations in reaction products ranged from 23.1 to 46.1 mmol Sr kg^{-1} solid (Table 1, Supporting Information). Control samples were analyzed after 10 months for dissolved organic carbon (Shimadzu TOC/TN) to determine CO_2 diffusion from the headspace and possibly the ambient air into reactant solutions. Details of experimental conditions and solution-phase chemistry are discussed in ref 17.

X-ray Diffraction (XRD) and Electron Microscopy. X-ray diffraction data were collected using a Philips X'pert MPD diffractometer with a spinning stage and X'Celerator multiple-strip detector with Ni-filtered Cu $K\alpha$ radiation at 50 kV and 40 mA. Representative samples were examined by scanning electron microscopy (SEM) coupled with energy-dispersive X-ray spectrometry (EDS) using either a FEI-Philips XL-20 or Hitachi S-2460N SEM at 25 kV. Transmission electron microscopy (TEM) was done with a Hitachi H8100 LaB₆ TEM operating at 200 kV. See Supporting Information for details.

Synchrotron X-ray Absorption Spectroscopy (XAS) Data Collection and Analysis. Strontium K-edge XAS fluorescence data for bulk samples were collected at the National Synchrotron Light Source (NSLS) on beamline X-18B (2.58 GeV, 300 mA) using an unfocused beam, a Si(111) monochromator crystal, and an Ar-filled Lytle detector. Spectra for two bulk samples (324 and 369 d-AAO) were collected at the Advanced Photon Source (APS) on GSECARS beamline 13-BM-D with a Si(111) monochromator crystal and a 16-element Ge fluorescence detector. Microfocused X-ray absorption spectra were collected at the Advanced Photon Source (APS) on GSECARS beamline 13-ID-C with a Si(111) monochromator crystal and a single-element SiLi fluorescence detector. Particles were dispersed on carbon tape and imaged with SEM to identify isolated Sr-bearing particles (distances between particles >1 μm) prior to synchrotron analyses. Extended X-ray absorption fine structure (EXAFS) data were analyzed by methods described previously (5). Theoretical reference functions were least-squares fit to experimental data on a shell-by-shell basis, varying distance (R), backscatterer number (N), and Debye–Waller factor (σ^2) (in some cases) for each atomic shell. See Supporting Information for details.

Results

Summary of Previous Experimental Results. Previous and concurrent studies of the kaolinite/STWL leachate system include analyses of the macroscopic solution chemistry and characterization of solid products by microscopic and

spectroscopic methods (17, 18). Both metals were present as co-contaminants at initial aqueous concentrations of 10^{-3} , 10^{-4} , and 10^{-5} mol kg^{-1} (all at 298 K), but EXAFS data were collected on samples only at the highest concentration. Reaction of kaolinite with STWL caused dissolution and release of Si and Al. Following initial increases in dissolved Si and Al, abrupt decreases after 7–33 d indicated precipitation of secondary aluminosilicate solids. The concentration of initial Cs and Sr in the STWL affected clay mineral dissolution rates and thus neophase precipitation. Solutions containing the highest dissolved Sr and Cs (10^{-3} mol kg^{-1}) had the slowest rates of Si and Al release. Strontium uptake exceeded that of Cs in both rate and extent, but both ions were increasingly recalcitrant to subsequent ion (Mg^{2+}) exchange or oxalic acid (AAO) dissolution treatments with aging. Previous characterization of solid products indicated the formation of nitrate sodalite, nitrate cancrinite, and Al-rich chabazite (17, 18).

X-ray Diffraction. Reacted kaolinite samples (10^{-3} mol kg^{-1} Sr and Cs) were re-analyzed by high-resolution XRD. As shown previously (17), unreacted samples indicate the presence of only kaolinite and no new diffraction peaks were identified in samples reacted up to 33 d. At 93 d of reaction, the presence of sodalite as a primary neophase was verified, along with characteristic reflections associated with cancrinite, which was not detected in the previous XRD analysis at this concentration. One or two characteristic reflections were present at 93, 190, and 324 d that were identified as Al- or Na-rich chabazite (Figure 1 in Supporting Information). However, chabazite peaks overlap other peaks and are not perfectly matched with Al-chabazite reference patterns. After extraction with AAO at 369 d, most reflections associated with sodalite and cancrinite were removed. Two peaks assigned to chabazite were still present in the diffractogram but were considerably reduced in amplitude (Figure 1 in Supporting Information).

Electron Microscopy and Energy Dispersive Spectrometry. Secondary phases formed after 33, 93, and 190 d of reaction were examined by SEM and TEM with elemental analysis from EDS (Figure 2 in Supporting Information). At 33 d, spheroidal particles with diameters of ~ 5 μm and no significant size variation among particles, contained Sr, some Cs, and a Si/Al ratio close to unity (from EDS peak heights). High Na concentrations were evident in addition to O and C (Figure 2a and b in Supporting Information) and analysis of multiple points showed little variation in relative composition. After 93 d of reaction, three different types of secondary phases were identified. Large particles (typically ~ 7 μm) had small but detectable amounts of Sr and Cs, and relatively lower Sr concentration than spheroidal particles at 33 d (Figure 2c in Supporting Information). Other particles had diameters under 2 μm and contained very high Sr and detectable Al (Si was masked by overlap with Sr $L\alpha$ emission peaks), but little or no C, Na, or Cs (Figure 2d in Supporting Information). Morphologically, these particles showed irregular edges compared to the other spheroidal particles. A third type of particle, with no detectable Sr and Cs but with Na and similar amounts of Si and Al, was about 2–5 μm in size and had a spheroidal morphology combined with platelike edges (Figure 2e in Supporting Information). Secondary particles observed at 193 d of reaction were similar to those at 93 d except that no highly concentrated Sr phases were found (Figure 2f and g in Supporting Information). Spheroidal phases without Sr and Cs had morphologies similar to those at 93 d and diameters of 2–5 μm . In general, EDS data indicated that secondary phases contained mostly Si and Al in about equal amounts, Na, and O, in addition to a smaller amount of C.

EXAFS Analysis of Bulk Samples. Fits of the Sr K-edge EXAFS spectra for bulk samples showed distinct changes as

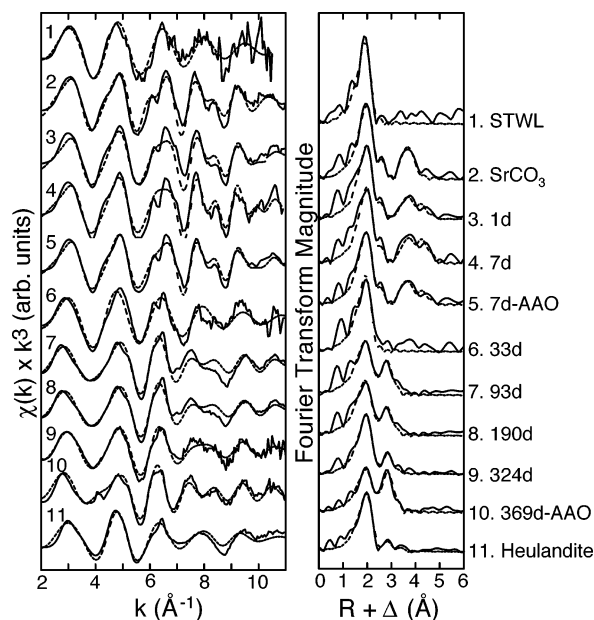


FIGURE 1. Normalized bulk Sr-EXAFS spectra and Fourier transforms (uncorrected for phase shift) of STWL/kaolinite reacted from 1 to 369 d (AAO: acidic ammonium oxalate extracted). Spectra are compared with published data for SrCO₃(s) and heulandite (5). Solid line, experimental data; dotted line, nonlinear least-squares fits (numerical results in Table 2 in Supporting Information).

a function of reaction time (Figure 1). The EXAFS spectrum of aqueous Sr in the STWL solution indicated Sr surrounded by a first shell of O atoms and no detectable second-neighbor atoms. The EXAFS fits of samples reacted for 1 and 7 d showed that the average local atomic structure around Sr was similar to that of crystalline SrCO₃(s) based on characteristic interatomic distances of near-neighbor atoms to ~4.9 Å (Table 2 in Supporting Information). The EXAFS spectrum of a 7 d sample treated with AAO has features very similar to those of the unextracted 7 d sample. Quantitative fits indicated a small reduction in amplitude (indicated by higher fitted Debye–Waller factors) but no change in interatomic distances within error (Table 2 in Supporting Information). The spectral features, interatomic distances, and Debye–Waller factors are very similar to those of a series of homogeneously and heterogeneously precipitated SrCO₃(s) samples that were analyzed by EXAFS previously (5, 6). Strontium carbonate phases were not detected by XRD or observed as distinct particles with electron microscopy in these samples. This result may imply a SrCO₃(s) precipitate with very small particle size or one that is present as a surface coating on kaolinite particles.

The bulk EXAFS spectrum for a kaolinite sample reacted for 33 d with STWL showed few features beyond the first O coordination shell around Sr in the Fourier transform (FT), although some features in the *k*-range of ~6–9 Å⁻¹ in the normalized EXAFS have similarities to the spectra at 1 and 7 d (Figure 1). Multiple trial-and-error fits, however, indicated that these features could not be fit quantitatively with statistical significance and thus, the 33 d spectrum was fit with a single O shell. Lack of distinct second-neighbor backscattering atoms may indicate that Sr is present primarily as a hydrated species, or may result from cancellation of backscattered wave functions if Sr is bonded in several sites of different coordination (e.g., multiple host phases). The difference between spectra collected at 1 and 7 d versus that collected at 33 d indicates that the carbonate phase is transient or of low abundance, with perhaps a trace amount of SrCO₃(s) detectable in the bulk EXAFS at 33 d based on spectral features similar to those at 1 and 7 d.

Bulk EXAFS spectra of kaolinite samples reacted for 93, 190, and 324 d, and an AAO-extracted, 369 d sample showed similar spectral features that differed from the spectra at 33 d or earlier (Figure 1). All spectra exhibit a first-shell O peak and second-neighbor backscattering that is best fit with Al or Si atoms (which cannot be distinguished in EXAFS backscattering because they differ by *Z* = 1). Trial-and-error-fit models demonstrated that the best fit for the STWL-reacted samples was a model with a single first-shell O distance and a single second-shell Sr–Al/Si distance at 3.43–3.46 Å (Table 2 in Supporting Information). This differs from fits to reference heulandite samples (Sr-bearing zeolite) that required an O shell and two different Sr–Al/Si distances (at 3.47–3.49 and 4.09–4.15 Å) to fit the spectra (5). Best fits to the bulk kaolinite spectra, however, showed some mismatch in the spectral region from *k* ~6.5–9 Å⁻¹ that could not be improved with the addition of a second Al/Si shell. This suggests disorder and the averaging of what is probably a range of Sr–Al/Si interatomic distances around ~3.4–3.5 Å. Based on the electron microscopy results, Sr is mostly associated with new aluminosilicate phases. The interatomic Sr–Al/Si distances from the EXAFS fits require partial dehydration of Sr and direct bonding to framework O atoms to produce the observed Sr–Al/Si distances. In the AAO-extracted sample at 369 d, the height of the Al/Si peak in the FT increases significantly compared to the unextracted 324 d spectrum, but the interatomic distance determined from the best fit was unchanged and the spectrum is better fit from *k* ~6.5–9 Å⁻¹ (Figure 1). These observations suggest that the fraction of Sr associated with more easily dissolved phases is hydrated, such that framework Al/Si atoms would be distant from Sr and not contribute scattering amplitude to the Sr–Al/Si peak at 3.46 Å. The stronger Al/Si backscattering in the AAO-extracted sample indicates dehydrated Sr and strong local bonding in a relatively crystalline aluminosilicate phase. Although XRD showed removal of sodalite and cancrinite peaks in the AAO extraction, the detection limit for XRD is on the order of 2–5 wt % for bulk phases, while EXAFS is sensitive to the residual Sr concentration in the extracted sample (6.38 mmol kg⁻¹, or 560 ppm Sr), well below the XRD detection limit.

Synchrotron Microfocused EXAFS and Microprobe Analysis. The bulk EXAFS spectrum of STWL-reacted kaolinite at 33 d showed no quantitatively analyzable features at atomic distances greater than the first O coordination shell, and no crystalline phases (other than kaolinite) by XRD. Imaging with SEM and TEM, however, revealed the presence of small, spherical neofomed particles with detectable concentrations of Sr. To further examine the Sr-bearing particles, we collected synchrotron microprobe maps and microfocused Sr-EXAFS of three individual particles within the 33 d sample (Figure 2). The particles were ~5 μm in diameter, and contained Sr and smaller amounts of Cs. Major elements were Al and Si in approximately equal concentrations and Na was observed in all particles. Figure 3 shows the EXAFS spectra of the individual particles compared to the bulk Sr EXAFS at 33 d. Although data quality is generally poorer in microfocused mode, differences in backscattering features among the spectra are apparent. Two of the microfocused spectra (33d-2 and 33d-3), which have a short data range (*k* = 2–10 Å⁻¹) and high noise levels, showed no or weak backscattering beyond the first O coordination shell (i.e., FT peaks at >2 Å with less amplitude than FT artifact peaks below the first-shell O peak), which is qualitatively similar to the result for the bulk spectrum (Figure 3). These spectra have possible scattering features at *k* ~8–10 Å⁻¹ but, given the noise levels of the data, they could not be fit quantitatively with a structurally reasonable fit model and thus may be artifacts. The lack of strong backscattering features beyond the first O coordination shell in microfocused spectra 33d-2 and 33d-3

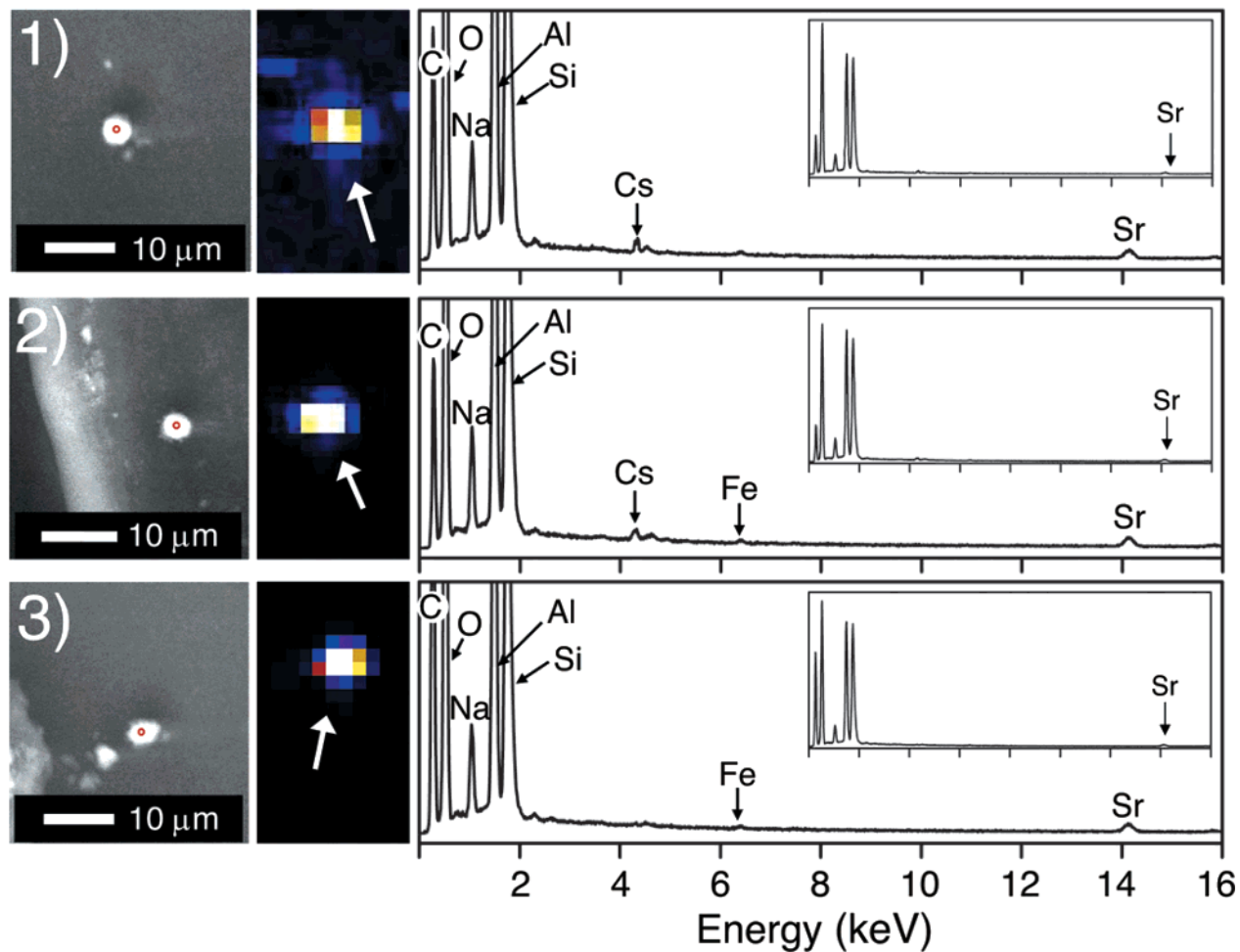


FIGURE 2. Backscattered electron images, synchrotron X-ray microprobe maps, and SEM-EDS of Sr-containing secondary phases after 33 d of STWL/kaolinite reaction. Spots shown in (1), (2), and (3) correspond to spectra 1, 2, and 3 in Figure 3.

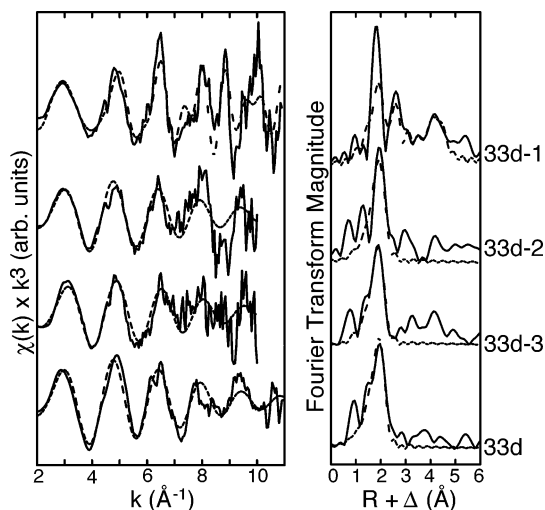


FIGURE 3. Microfocused Sr-EXAFS spectra and Fourier Transforms (uncorrected for phase shift) of particles from 33 d STWL/kaolinite sample; 1, 2, and 3 correspond to images shown in Figure 2. Bulk spectrum at 33 d from Figure 1. Solid line, experimental data; dotted line, nonlinear least-squares fits (numerical results in Table 3 in Supporting Information).

are interpreted as a predominance of Sr environments where Sr atoms are primarily coordinated by water or hydroxyl ligands.

One of the spectra (33d-1) showed strong backscattering features at distances beyond the first atomic shell with a unique EXAFS pattern (Figure 3). Trial-and-error fits showed that two Al/Si distances, 3.34 and 3.55 Å (which partially overlap and cancel) were needed to fit the spectrum, rather than one as in the bulk spectra for more aged samples. Scattering at long interatomic distances, which gives rise to the strong features at $k > 8 \text{ \AA}^{-1}$ (between 4 and 5 Å in the FT), results only from high Z atoms (scattering from low Z atoms is typically too weak at such distances in room temperature spectra to produce EXAFS). Least-squares fits assuming Sr coordination in feldspathoid or zeolite phases identified from XRD of samples at 190 and 324 d (sodalite, cancrinite, or chabazite) are consistent with the presence of second-neighbor Sr and/or Cs atoms in adjacent extraframework cation sites in these minerals. The spectrum could be reasonably fit with either Sr or Cs in neighboring cation sites in the range of $\sim 4.4\text{--}4.8 \text{ \AA}$ and suggests a mixture, which is consistent with EDS data. These high- k features could not be fit assuming Na in the backscattering cation site. Although Na is probably present in these sites, its scattering amplitude at these distances is much weaker than that of Sr or Cs. Overall, the microfocused and bulk EXAFS spectra at 33 d indicate that Sr is present in neofomed aluminosilicate phases as both hydrated and dehydrated Sr in different proportions within particles. The microfocused spectrum suggests clustering of heavy Sr and/or Cs atoms in adjacent cation sites in some particles.

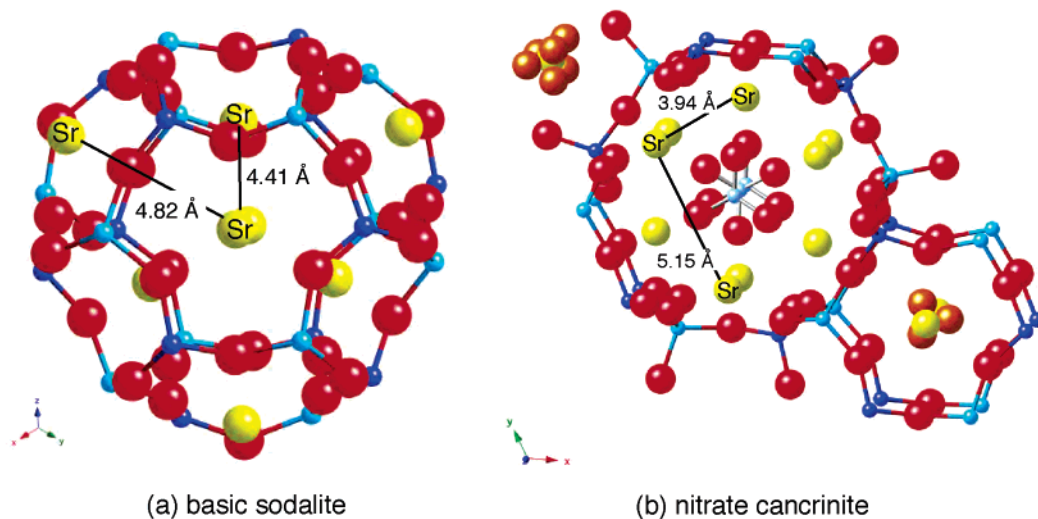


FIGURE 4. (a) Atomic structure of basic sodalite (21) with a single cage and cation site. Sr (yellow atoms) occupies the Na site; surrounding anions and water within cages are omitted for clarity; (b) Nitrate cancrinite (23) has two distinct cation sites in large (sodalite-type) and small (cancrinite-type) cages; Sr is shown occupying Na sites within the sodalite cage, nitrate groups occupy the counteranion position in the center of the cage, and Na and water are shown in the cancrinite cage. Nearest interatomic cation–cation positions are indicated.

Discussion

Incorporation of Sr into Reaction Products. The results of product characterization, together with previous analysis of changes in solution chemistry (17), indicate a reaction progress for Sr that is controlled by the formation of secondary phases and is dependent on the rate of dissolution and release of Si from kaolinite. At Sr and Cs concentrations of 10^{-3} mol kg^{-1} , Sr EXAFS spectra at 1 and 7 d indicate formation of a Sr phase with the local structure of $\text{SrCO}_3(\text{s})$ that is not easily dissolved, even though this phase was below detection by XRD and was not observed by SEM or TEM. Although CO_2 was minimized in the reactant solutions, diffusion of ambient CO_2 into solutions during sample preparation and reaction was not prevented. Solution control samples (STWL with Sr and Cs but no kaolinite) showed no visible signs of precipitate formation and no loss of Sr from solution. After 10 months of equilibration, total inorganic carbon (TIC) in solution controls with and without dissolved Al varied from 0.9 to 2 mM. At the ionic strength and pH of the STWL solutions, dissolved ion activities are greatly reduced due to significant complex formation and activity coefficients $\ll 1$. For example, speciation calculations of tank solutions using Pitzer activity corrections suggested that divalent free ion activities may be reduced by over 2 orders of magnitude in tank wastes (at ionic strengths of ~ 3.5 mol kg^{-1}) (19). We estimate that solutions approached the equilibrium solubility of $\text{SrCO}_3(\text{s})$ ($\log K_{\text{eq}} = -9.27$ at 25°C ; (9)) at Sr concentrations of 10^{-3} mol kg^{-1} , depending on the amount of dissolved carbonate actually present. Although TIC concentration was not measured at 1 or 7 d, it was presumably less than or equal to the maximum (2 mM) measured after 10 months. The lack of observed precipitation in kaolinite-free control solutions points to the role of the kaolinite surface in promoting precipitation, perhaps by adsorption of carbonate as suggested for goethite and other minerals in previous studies (6, 8). The formation of a $\text{SrCO}_3(\text{s})$ surface precipitate at 10^{-3} mol kg^{-1} Sr could account for the slower dissolution rate of kaolinite under these conditions by blocking surface sites from hydroxide attack, compared to experiments conducted at 10^{-4} and 10^{-5} mol kg^{-1} Sr (17, 18) in which it is likely that $\text{SrCO}_3(\text{s})$ remained undersaturated.

By 33 d of reaction, bulk EXAFS data indicate that the $\text{SrCO}_3(\text{s})$ phase is transient or at low relative abundance, and that hydrated Sr is dominant over dehydrated Sr on average. However, SEM/TEM/EDS analyses indicated that most Sr is

strongly associated with distinct spherical particles and not randomly distributed on all surfaces, which would be expected if Sr was primarily adsorbed to mineral surfaces. Microfocused EXAFS of three different particles at 33 d, all with a similar spherical morphology observed by SEM, indicated both hydrated and dehydrated Sr based on the presence or absence of Al/Si and Sr/Cs backscatterers. Evidence from SEM/TEM, FTIR (17), and NMR (18) studies indicated the emergence at 33 d of a new phase identified as a disordered sodalite-type mineral. For comparison, we consider the well-known structure of crystalline sodalite, which is cubic with a single, symmetric, extraframework cation site (X) that gives rise to a single interatomic X–Al/Si distance from six Al or Si framework atoms (e.g., Na–Si/Al = 3.30 Å in nitrate sodalite, ideally $\text{Na}_6(\text{AlSiO}_4)_6(\text{NO}_3)_2 \cdot 2\text{H}_2\text{O}$ (20), and 3.35 Å in basic sodalite where OH^- substitutes for NO_3^- (21)) (Figure 4a). The presence of two distinct Sr–Al/Si distances from the EXAFS fit (Table 3 in Supporting Information) indicates the lack of a single symmetric Sr site, which is not consistent with the structure of ideal, crystalline sodalite. Nearest adjacent cation sites in Na sodalites (X–X distances) are 4.73 and 4.85 Å in nitrate sodalite and 4.41 and 4.82 Å in basic sodalite. The Sr–Sr/Cs interatomic distances of 4.37 and 4.77 Å from the EXAFS fit (Table 3 in Supporting Information) are within the range expected for backscattering from an adjacent extraframework site. Cancrinite, which is polymorphic with sodalite but crystallizes in a hexagonal space group, has two distinct cation sites associated with large (sodalite-type) and small (cancrinite-type) cages (22, 23). This structure has a larger range of interatomic cation–cation distances than does sodalite (X–X = 3.94–5.55 Å in ideal nitrate cancrinite) (Figure 4b). The bulk and microfocused spectra suggest different populations of Sr attributed to the following: (1) hydrated Sr within sodalite-type cages as the dominant fraction, and (2) dehydrated Sr in either a single, asymmetric site, giving rise to two Sr–Al/Si distances, or at least two symmetric sites with different Sr–Al/Si distances. The discrepancies between interatomic distances determined from EXAFS analysis and from published XRD structure determinations indicate that the neoformed phases binding Sr are not ideal, crystalline sodalite or cancrinite at 33 d. Stepwise chemical extractions of the 33 d sample showed that the fraction of readily exchangeable Sr dominated (65%) over the pools of AAO-extractable (22%) and strongly bound Sr (13%) (17), consistent with the EXAFS

interpretation of hydrated and dehydrated Sr associated with new sodalite-type phases.

With longer reaction times, evidence from NMR, XRD, SEM/TEM, and FTIR indicates the formation of both sodalite and cancrinite, with cancrinite forming at the expense of sodalite for reaction times longer than 93 d (17, 18). The XRD data also indicate the formation of a third phase identified as an Al-rich chabazite beginning at 93 d. Extractions of samples reacted for 93–369 d showed that most sorbed Sr (70–80%) was not extractable with AAO treatment (17). The Sr-EXAFS spectra for all samples aged more than 33 d can be fit with a single Sr–Al/Si distance (3.43–3.46 Å), indicating migration of Sr into a more symmetric cation site on average. The increase in amplitude of the Al/Si peak without a change in bond distance in the AAO-extracted, 369 d sample indicates a higher proportion of dehydrated than hydrated (exchangeable) Sr associated with a more crystalline phase than at 33 d. The lack of scattering from Sr or Cs atoms in adjacent cation sites in the aged samples also indicates evolution to an ordered structure where Na, Cs, and Sr are more widely spaced within aluminosilicate cages. These observations are consistent with electron microscopy and EDS that showed similar Sr and Cs concentrations in uniform, spherical particles at 190 d and longer reaction times. Electron microscopy and EDS indicated that particles with platy morphology, identified as nitrate–cancrinite (17), contained Na but lacked significant Sr and Cs (Figure 2 in Supporting Information). Together with the EXAFS, this evidence points to incorporation of Sr into a regular site such as the single cation site in sodalite as the system ages (Figure 4). Some Sr may be associated with the chabazite-type phase identified by XRD, which also has symmetric cation sites that can accommodate Sr.

Implications for Contaminant Uptake and Release. The STWL/kaolinite experimental system lends mechanistic insight into a possible reaction history of caustic wastes and natural clay minerals that occurred, for example, in the near-field conditions associated with leaking underground waste storage tanks at Hanford in which the initial concentrations of radioactive contaminants were variable (3). At high Sr concentrations (10^{-3} mol kg⁻¹), the earliest detectable new product is SrCO₃(s), which may be present as small particles and/or surface coatings. The kinetics of SrCO₃(s) precipitation is fast, as shown by its immediate formation (1 d) in our system and in previous investigations at ambient CO₂ in unaged samples (6). Because of the larger ionic radius of Sr²⁺ compared to Ca²⁺, SrCO₃ (strontianite) is isostructural with aragonite rather than calcite and the extent of Sr²⁺ incorporation into calcite is limited to trace amounts. Although isostructural, experimental studies have demonstrated a large miscibility gap in the aragonite–strontianite solid solution (9). In calcium carbonates with high Sr (more than ~5000 ppm), spectroscopic evidence suggested the presence of micro- or nanoscale SrCO₃(s) domains (24). In the near-field subsurface where carbonate is not limited, SrCO₃(s) is a likely early product if its solubility is exceeded from high Sr concentrations in the tank waste. If SrCO₃(s) is undersaturated because of lower initial concentrations and Sr substitution into calcite is limited, then adsorption of Sr²⁺ on existing mineral surfaces, most likely as an outer-sphere complex (5–7), is the only other kinetically fast uptake mechanism. Re-release of Sr²⁺ to solution as pH decreases will depend on whether solutions become undersaturated with respect to carbonate minerals, how much Sr was incorporated into carbonate versus adsorbed, and the rate of dissolution.

As kaolinite dissolution progressed and aqueous Si concentrations increased in our experimental system, Sr was incorporated into nucleating feldspathoid phases, with nearly complete Sr removal from solution. As shown previously, the rate of formation of new aluminosilicate phases depended

on the rate of Si release from kaolinite and was inhibited at high Sr concentrations (17, 18), presumably because of the formation of a SrCO₃(s) surface precipitate. The earliest aluminosilicate phases at 33 d were probably disordered sodalite-group minerals (18). The sodalite–cancrinite group is a diverse family of structurally related minerals that contain aluminosilicate framework cages of different sizes, generating a large number of extraframework sites. The extraframework sites can accommodate ions of different size and charge, and they may or may not be fully occupied with cations, anions, and/or water (25). Substitution of divalent cations into monovalent cation sites in sodalite-group minerals requires coupled cation/anion substitution or substitution of water for anions if Al/Si remains at 1:1. In general for synthetic aluminosilicates, the lower the synthesis temperature, the higher the intracrystalline void volume and the higher the water content (26). Thus, during their initial formation in the STWL–kaolinite system, aluminosilicate neophases may be poorly crystalline mixtures of cages of different size that nucleated around structure-directing, cation/anion pairs and water. The role of Sr²⁺ and Cs⁺ in directing the nucleation of sodalite-group phases is suggested by the microfocused EXAFS spectrum in which Sr or Cs occupy cation sites within close proximity (~4.4–4.8 Å) to other Sr atoms. Multiple Sr–Al/Si distances in the EXAFS indicate occupation of either asymmetric or multiple extraframework sites. As the system ages, more crystalline sodalite and cancrinite phases form, with evidence for exclusion of Sr and possibly Cs from cancrinite, and greater recalcitrance of Sr to extraction, which arises from its dehydration and direct bonding to framework Al and Si. This may reflect partial collapse of the aluminosilicate framework around cation–anion pairs within sodalite cages that irreversibly trap extraframework ions and water, as seen in synthetic hydrosodalite phases (27). Because guest ions are strongly bonded and generally resistant to desorption, particularly divalent ions, re-release to solution requires dissolution of the host feldspathoid phase.

Although this experimental system is greatly simplified from field conditions, an important observation is that the largely irreversible trapping of radionuclides can occur if they are present during the formation and aging of feldspathoid phases as alteration products of local Si-bearing sediment minerals. The effectiveness of such a coprecipitation mechanism for contaminant sequestration, as opposed to exchange or adsorption on existing clay or zeolite minerals, depends on the relative rates associated with the mechanistic steps: native mineral dissolution to supply Si, precipitation of secondary feldspathoids, and dehydration of guest ions and cage collapse. Based on this experimental system and similar studies with 2:1 specimen clays (15, 16), the time scale of the overall process is on the order of weeks to months, and is most influenced by the supply of Si to the system from clay mineral dissolution. Sequestration of radionuclides by feldspathoid mineral trapping may be an important mechanism for irreversible retardation near waste sources because re-release to solution requires mineral dissolution rather than ion exchange. As caustic waste fluids are neutralized away from sources, silicate mineral dissolution rates decrease and competing processes, such as the formation of carbonate minerals and adsorption, are expected to become dominant.

Acknowledgments

We thank Matt Newville (GSECARS) for invaluable assistance with XAS data collection and Jason Field for additional assistance. Two anonymous reviewers provided helpful comments on the manuscript. Portions of this work were performed at GSECARS (Sector 13, APS), Argonne National Laboratory, which is supported by the NSF (EAR-0217473), the U.S. DOE (DE-FG02-94ER14466), and the State of Illinois.

The APS is supported by the U.S. DOE-BES (W-31-109-Eng-38). Research was carried out in part at the NSLS, Brookhaven National Laboratory, which is supported by the U.S. DOE (DE-AC02-98CH10886). This study was supported by the U.S. DOE (DE-FG07-02ER63504).

Supporting Information Available

Additional information about materials and methods used in this study; X-ray diffractograms, electron microscopy images, and quantitative results of EXAFS fits. This material is available free of charge via the Internet at <http://pubs.acs.org>.

Literature Cited

- (1) Department of Energy. *Report to Congress, Top-to-Bottom Review of Environmental Management Program: Status of Implementation*; 2003.
- (2) Gephart, R. E. *Hanford, A Conversation About Nuclear Waste and Cleanup*; Battelle Press: Columbus, OH, 2003.
- (3) Serne, R. J.; Bjornstad, B. N.; Horton, D. G.; Lanigan, D. C.; Lindenmeier, C. W.; Lindberg, M. J.; Clayton, R. E.; LeGore, V. L.; Geiszler, K. N.; Baum, S. R.; Valenta, M. M.; Kutnyakov, I. V.; Vickerman, T. S.; Orr, R. D.; Brown, C. F. *Characterization of vadose zone sediments below the T Tank farm: Boreholes C4104, C4105, 299-W10-196 and RCRA borehole 299-W11-39*. PNNL: Richland, WA, 2004; PNNL-14849.
- (4) Kaplan, D. I.; Parker, K. E.; Orr, R. D. *Effects of high pH and high ionic strength groundwater on iodide, pertechnetate and selenate sorption to Hanford sediments: Final report for subtask 3a*. PNNL: Richland, WA, 1998; PNNL-11964.
- (5) O'Day, P. A.; Newville, M.; Neuhoff, P. S.; Sahai, N.; Carroll, S. A. X-ray absorption spectroscopy of strontium(II) coordination – I. Static and thermal disorder in crystalline, hydrated, and precipitated solids and in aqueous solution. *J. Colloid Interface Sci.* **2000**, *222*, 184–197.
- (6) Sahai, N.; Carroll, S. A.; Roberts, S.; O'Day, P. A. X-ray absorption spectroscopy of strontium(II) coordination – II. Sorption and precipitation at kaolinite, amorphous silica, and goethite surfaces. *J. Colloid Interface Sci.* **2000**, *222*, 198–212.
- (7) Um, W.; Papelis, C. Sorption mechanisms of Sr and Pb on zeolitized tuffs from the Nevada test site as a function of pH and ionic strength. *Am. Mineral.* **2003**, *88*, 2028–2039.
- (8) Catalano, J. G.; Brown, G. E. Uranyl adsorption onto montmorillonite: Evaluation of binding sites and carbonate complexation. *Geochim. Cosmochim. Acta* **2005**, *69*, 2995–3005.
- (9) Plummer, L. N.; Busenberg, E. Thermodynamics of aragonite-strontianite solid-solutions – Results from stoichiometric solubility at 25-degrees-C and 76-degrees-C. *Geochim. Cosmochim. Acta* **1987**, *51*, 1393–1411.
- (10) McKinley, J. P.; Zachara, J. M.; Heald, S. M.; Dohnalkova, A.; Newville, M. G.; Sutton, S. R. Microscale distribution of cesium sorbed to biotite and muscovite. *Environ. Sci. Technol.* **2004**, *38*, 1017–1023.
- (11) Kim, Y.; Kirkpatrick, R. J.; Cygan, R. T. Cs-133 NMR study of cesium on the surfaces of kaolinite and illite. *Geochim. Cosmochim. Acta* **1996**, *60*, 4059–4074.
- (12) Bostick, B. C.; Vairavamurthy, M. A.; Karthikeyan, K. G.; Chorover, J. Cesium adsorption on clay minerals: An EXAFS spectroscopic investigation. *Environ. Sci. Technol.* **2002**, *36*, 2670–2676.
- (13) Qafoku, N. P.; Ainsworth, C. C.; Szecsody, J. E.; Bish, D. L.; Young, J. S.; McCready, D. E.; Qafoku, O. S. Aluminum effect on dissolution and precipitation under hyperalkaline conditions: II. Solid-phase transformations. *J. Environ. Qual.* **2003**, *32*, 2364–2372.
- (14) Wan, J. M.; Tokunaga, T. K.; Larsen, J. T.; Serne, R. J. Geochemical evolution of highly alkaline and saline tank waste plumes during seepage through vadose zone sediments. *Geochim. Cosmochim. Acta* **2004**, *68*, 491–502.
- (15) Choi, S.; Amistadi, M. K.; Chorover, J. Clay mineral weathering and contaminant dynamics in a caustic aqueous system. I. Wet chemistry and aging effects. *Geochim. Cosmochim. Acta* **2005**, *69*, 4425–4436.
- (16) Choi, S.; Crosson, G.; Mueller, K. T.; Seraphin, S.; Chorover, J. Clay mineral weathering and contaminant dynamics in a caustic aqueous system. II. Mineral transformation and microscale partitioning. *Geochim. Cosmochim. Acta* **2005**, *69*, 4437–4451.
- (17) Chorover, J.; Choi, S.; Amistadi, M. K.; Karthikeyan, K. G.; Crosson, G.; Mueller, K. T. Linking cesium and strontium uptake to kaolinite weathering in simulated tank waste leachate. *Environ. Sci. Technol.* **2003**, *37*, 2200–2208.
- (18) Crosson, G. S.; Choi, S.; Chorover, J.; Amistadi, M. K.; O'Day, P. A.; Mueller, K. T. Solid-state NMR identification and quantification of newly formed aluminosilicate phases in weathered kaolinite systems. *J. Phys. Chem. B* **2006**, *110*, 723–732.
- (19) Lichtner, P. C.; Felmy, A. R. Estimation of Hanford SX tank waste compositions from historically derived inventories. *Comput. Geosci.* **2003**, *29*, 371–383.
- (20) Buhl, J. C.; Lons, J. Synthesis and crystal structure of nitrate enclathrated sodalite $\text{Na}_8[\text{AlSiO}_4]_6(\text{NO}_3)_2$. *J. Alloys Compd.* **1996**, *235*, 41–47.
- (21) Hassan, I.; Grundy, H. D. Structure of basic sodalite, $\text{Na}_6\text{Al}_6\text{Si}_6\text{O}_{24}(\text{OH})_2 \cdot 2\text{H}_2\text{O}$. *Acta Crystallogr. C* **1983**, *39*, 3–5.
- (22) Hassan, I.; Grundy, H. D. The crystal structure of basic cancrinite, ideally $\text{Na}_8[\text{Al}_6\text{Si}_6\text{O}_{24}](\text{OH})_2 \cdot 3\text{H}_2\text{O}$. *Can. Mineral.* **1991**, *29*, 377–383.
- (23) Fechtelkord, M.; Posnatzki, B.; Buhl, J. C.; Fyfe, C. A.; Groat, L. A.; Raudsepp, M. Characterization of synthetic Cs–Li cancrinite grown in a butanediol-water system: An NMR spectroscopic and Rietveld refinement study. *Am. Mineral.* **2001**, *86*, 881–888.
- (24) Gregor, R. B.; Pingitore, N. E.; Lytle, F. W. Strontianite in coral skeletal aragonite. *Science* **1997**, *275*, 1452–1454.
- (25) Depmeier, W. The sodalite family – A simple but versatile framework structure. In *Micro- and Mesoporous Mineral Phases*; Ferraris, G., Merlino, S., Eds.; Mineralogical Society of America: Washington, DC, 2005; Vol. 57, pp 203–240.
- (26) Davis, M. E.; Lobo, R. F. Zeolite and molecular-sieve synthesis. *Chem. Mater.* **1992**, *4*, 756–768.
- (27) Kendrick, E.; Dann, S. Synthesis, properties and structure of ion exchanged hydrosodalite. *J. Solid State Chem.* **2004**, *177*, 1513–1519.

Received for review September 20, 2005. Revised manuscript received February 16, 2006. Accepted February 17, 2006.

ES051869Q